



HAL
open science

Large-scale volcanic deposit fluidization by dilute pyroclastic density currents

Karim Kelfoun, Antonio Proaño

► **To cite this version:**

Karim Kelfoun, Antonio Proaño. Large-scale volcanic deposit fluidization by dilute pyroclastic density currents. *Nature Geoscience*, 2023, 16 (6), pp.499-504. 10.1038/s41561-023-01190-7. hal-04215005

HAL Id: hal-04215005

<https://uca.hal.science/hal-04215005>

Submitted on 22 Sep 2023

HAL is a multi-disciplinary open access archive for the deposit and dissemination of scientific research documents, whether they are published or not. The documents may come from teaching and research institutions in France or abroad, or from public or private research centers.

L'archive ouverte pluridisciplinaire **HAL**, est destinée au dépôt et à la diffusion de documents scientifiques de niveau recherche, publiés ou non, émanant des établissements d'enseignement et de recherche français ou étrangers, des laboratoires publics ou privés.

Large-scale volcanic deposit fluidisation by dilute pyroclastic density currents

Published in *Nature Geoscience*, 2023

DOI - <https://doi.org/10.1038/s41561-023-01190-7>

Karim Kelfoun¹, Antonio Proaño^{1,2}

1. Université Clermont Auvergne, CNRS, IRD, OPGC, Laboratoire Magmas et Volcans, F-63000 Clermont-Ferrand, France. Corresponding author: karim.kelfoun@uca.fr
2. Instituto de Investigación Geológica y Energética (IIGE), Quito 170503, Ecuador

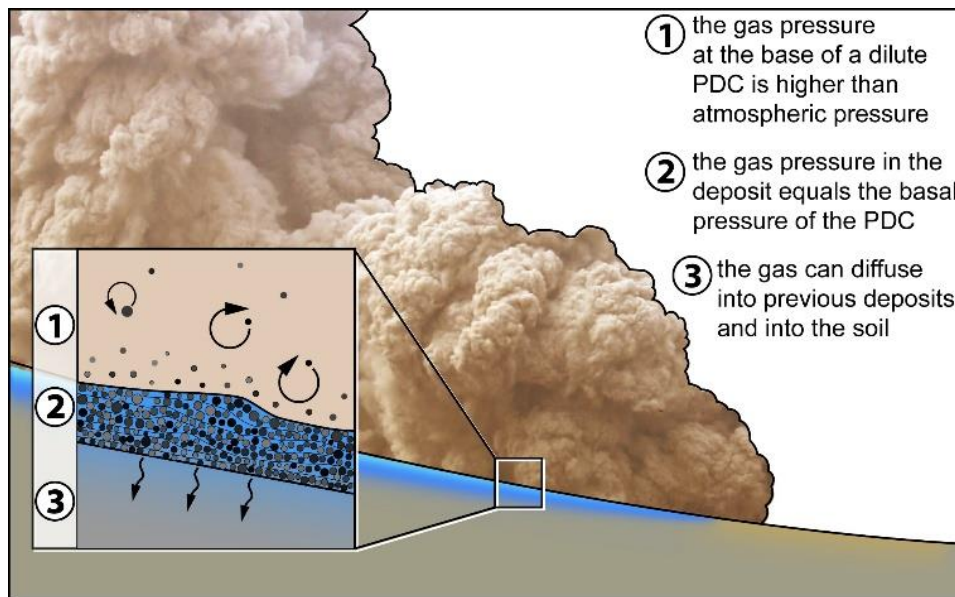
Introductory paragraph

There is increasing evidence that fine-grained deposits of pyroclastic density currents can be remobilized on a large scale, resulting in concentrated flows. These flows can be a major hazard: for example, at Soufrière Hills Volcano (Montserrat) in 1997, some travelled beyond the designated danger zone to inhabited areas. Despite their hazard potential, the scale and generation mechanism of these flows are poorly understood. Here we demonstrate using laboratory experiments and numerical modelling that decompression following the passage of dilute pyroclastic density currents can cause rapid deposit fluidization over areas of several square kilometres and to depths of tens of centimetres. The fluidized volume can be substantially greater than that deposited by the triggering pyroclastic density current because of remobilization of previously emplaced deposits, and the fluidized volume can flow even on slopes of a few degrees. The capacity for remobilization of a deposit is limited by its particle cohesion, which rapidly increases with atmospheric humidity. This mechanism of fluidisation should alert us to an under-appreciated volcanic hazard of long-runout pyroclastic flows that can be generated by remobilisation very rapidly and with little warning.

Main

Ground-hugging pyroclastic density currents (PDCs) are made up of a mixture of gas and volcanic particles. They cover a broad spectrum of densities from dilute to concentrated. Dilute currents, also called *nuées ardentes* and pyroclastic surges¹⁻³, transport particles predominantly by turbulent suspension⁴. These currents may originate at an eruptive vent or as the turbulent cloud atop a concentrated PDC. Their particle concentrations are relatively low (< 5%⁵⁻⁷) except close to the ground, where they increase² and where particles are deposited through bed-load mechanisms (such as saltation, traction and rolling)³. Dilute PDCs easily escape any valley topography to cover the interfluves over large areas (several km²)⁸⁻¹¹. Field evidence such as slumps, overturned deposit laminations and block sag structures (ref¹² and therein) show that the deposits formed by dilute PDCs can experience a fluid behaviour locally. The deposits can be in such a fluid state that coarse ash grains falling onto them forms tiny sag structures¹³. At a much larger scale, the fluidity could affect extensive areas, up to several hundred square metres, and, on slopes, the remobilized deposit could evolve into a concentrated flow able to move hundreds to thousands of metres independent of the parent dilute PDC. This phenomenon, called surge-derived pyroclastic flow, was observed particularly well at Montserrat in 1997^{14,15}, and where also documented at Mount St Helens^{16,17}, Montagne Pelée¹⁸, Merapi¹¹ and at phreatomagmatic Ubehebe Crater^{12,13,19}. Among the various mechanisms evoked for localised fluidisation (ref¹² and therein), the role of pore gases is thought to be highly influential. Field evidence, such as segregation pipes and surface craters, indicate gas defluidisation after emplacement^{3,11,16,20}. The current explanation for large-scale remobilisation is that gases are trapped during rapid sedimentation of the dilute PDC^{13,15}. As with the dramatic large-scale liquefaction by water²¹⁻²⁷, the pressure gradient between the pressurized interior of the deposit and the surface could counterbalance the weight of the particles²⁸⁻³⁴. The normal stress between the particles drops and, consequently, the resisting shear stress decreases too. If the pressure gradient is steep enough, then the deposit behaves as a fluid and, especially on steep slopes, can begin to flow. However, it is not clear how such an

55 overpressure builds up. Indeed, while a densely-packed deposit of fine particles can retain
56 gases^{32,35}, the spaces between the particles probably allow the gas to escape when the particles
57 settle out of the dilute PDC except at very high settling rates^{34,36} that seem incompatible with
58 their runouts and the mass of particles transported.
59



60
61 **Figure 1.** Emplacement of a dilute PDC. (a) The pressure of the gas, at its base, is higher than atmospheric pressure.
62 Consequently, it is higher in the resulting deposit. This induces deposit fluidisation in the aftermath of the PDC,
63 when the surface pressure drops back down rapidly enough.
64
65

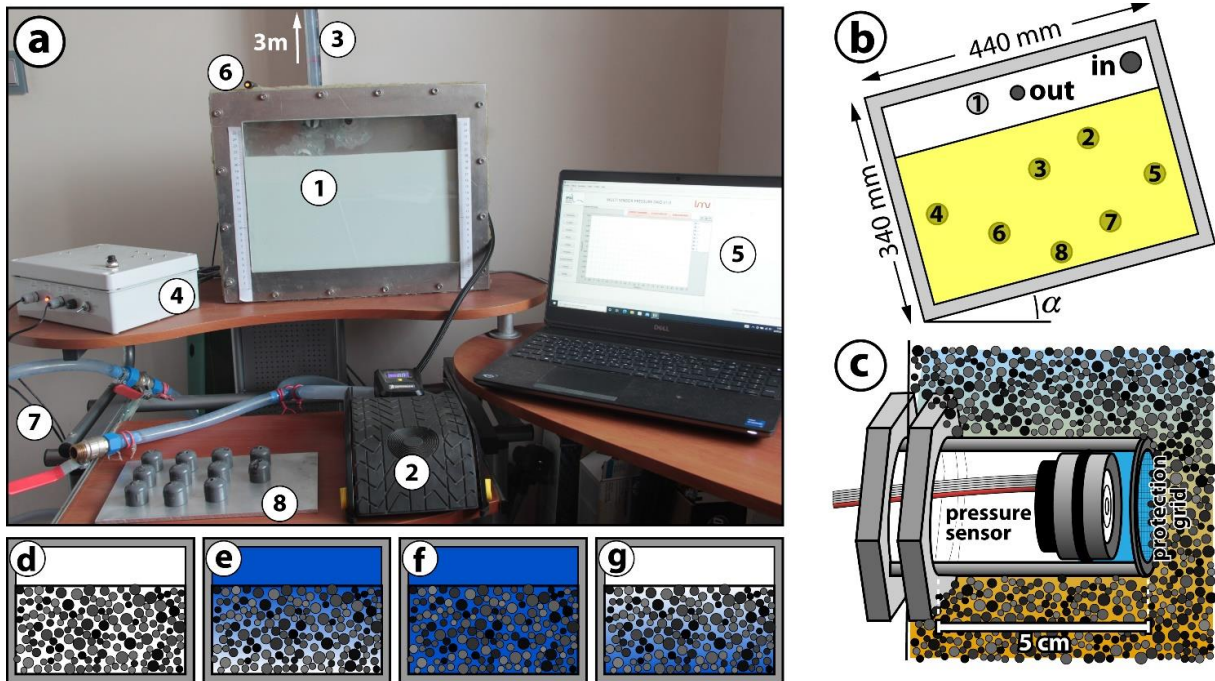
66 One characteristic of dilute PDCs has not been studied up to now: due to their depth, density
67 and velocity, the gas pressure at their base is higher than atmospheric pressure. The pressure of
68 the interstitial gas in the deposits they form is thus also higher (Fig 1). After the passage of a
69 PDC, the pressure of the gas at the surface must drop back to atmospheric pressure. A gas
70 pressure gradient is thus temporarily created between the interior of the deposit and its surface.
71 Is this pressure gradient enough to fluidise the deposit? What might the consequences of this
72 type of fluidisation be?

73 To answer these questions, we designed an experimental pressurized tank (see Methods) filled
74 with granular material (Fig 2). Pressure sensors in the granular bed measure the air pressure at
75 different depths. To ensure that the observed phenomena reproduce conditions that could also
76 occur in the field, the experiment setup has been scaled to nature in term of overpressure,
77 deposit thickness and particle permeability. We also developed a numerical model to further
78 explore the larger range of parameters found in actual volcanic fields.
79

80 **Range of parameters studied**

81 Particles deposited by dilute PDCs typically ranges from tens of microns to a few
82 millimetres^{11,20,37}. The gas permeability K , related to the particle size, can be as low as 10^{-13} –
83 5×10^{-12} m² in ignimbrite and pumice deposits^{35,38}. For deposits of dilute PDC and surge-derived
84 pyroclastic flows, K has been estimated between 10^{-11} and 10^{-10} m² although the finest particles
85 found in these deposits ($< 20 \mu\text{m}$) can significantly lower this value^{11,20,38,39}. Dilute PDC
86 deposits is typically of some centimetres to tens of centimetres thick^{11,19,20}. Because they may
87 overlie previous deposits into which the gas can diffuse, we have explored deposit thicknesses
88 H of up to 10 m. We have also explored a large range of deposit densities ρ , between 500 to
89 2000 kg/m^3 . The air viscosity is between $\mu = 1.85 \times 10^{-5}$ (at 20°C) and 4.5×10^{-5} Pa s (at 950°C).

90 The maximal static gas pressure at the base of a moderate PDC and its unloading time (i.e. the
 91 time to drop back from the maximal static pressure to atmospheric pressure) can be estimated
 92 indirectly through numerical simulations of PDC emplacement at Merapi⁴⁰ and Montserrat⁴¹ at
 93 5–10 kPa and 5–30 s, respectively. However, the total gas pressure at the base of a PDC must
 94 also include the dynamic pressure which depends on the PDC density ρ_s and its velocity u_s , and
 95 is given by $\frac{1}{2}\rho_s u_s^2$. The maximal particle concentration carried by turbulence in a dilute PDC
 96 is about 5% vol.^{5–7} i.e. a density of about $\rho_s = 70 \text{ kg/m}^3$. With a velocity of 40 m/s^{42,43}, the
 97 dynamic pressure increases by more than 50 kPa at certain places where the current meets rises
 98 in topography. Moreover, turbulence can create fluctuations in pressure of up to three times that
 99 of the mean dynamic pressure⁴⁴. These pressure fluctuations can also cause higher than
 100 expected unloading rates. To take these uncertainties into account, we have explored a large
 101 range of initial basal pressures P_{s0} (1–100 kPa) over the atmospheric pressure (P_{atm}), a large
 102 range of unloading times Δt (0–300 s) and, consequently, a large range of unloading rates (10
 103 Pa/s to >20 kPa/s).
 104

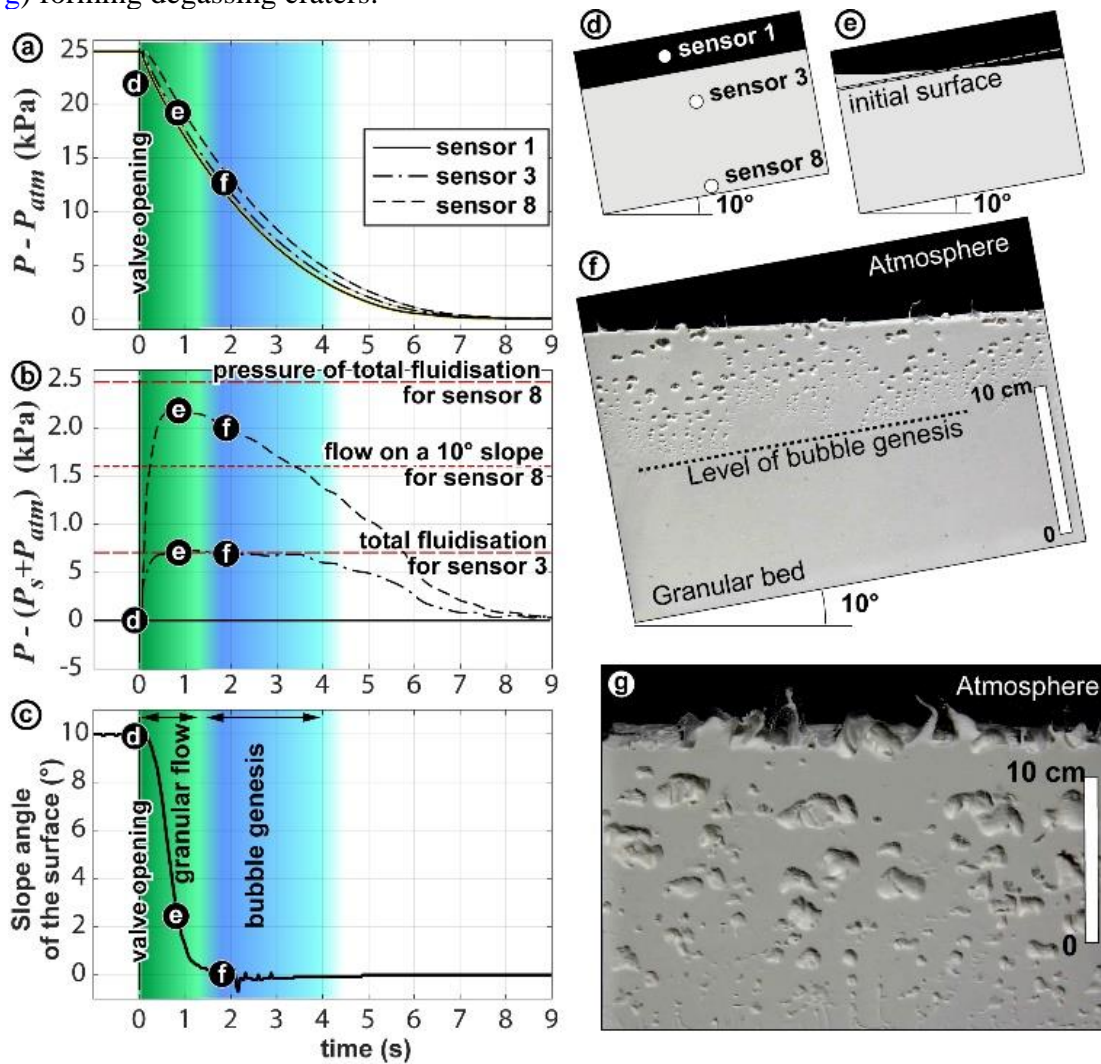


105 **Figure 2:** The experimental device made to simulate the unloading of a dilute PDC. (a) (1) the sealed tank partially
 106 filled with granular material, (2) pump, (3) vertical pipe filled with water for sensor calibration, (4) acquisition
 107 device, (5) computer and our dedicated acquisition software, (6) LED for synchronisation of videos and pressure
 108 measurements, (7) depressurisation valve, (8) pierced caps. (b) Locations of the pressure sensors, numbered 1–8.
 109 (c) Schematic representation of one of the sensors used to measure the gas pressure at various depths in the granular
 110 bed (located on 2b). (d) Initially, the air between the particles and that above is at atmospheric pressure. (e) The
 111 air is then pressurised (using a pump (2) in (2a) and diffuses between the particles. (f) When the pressure is
 112 equalized, the valve (7) in (2a) is opened. A cap (8) in (2a) screwed on to the valve controls the decompression
 113 rate. Decompression is slower between the particles than above them. (g) This creates a pressure gradient that can
 114 fluidise the particle bed.
 115
 116

117 Experimental results

118 The experimental procedure is described in the [Methods](#) section. The air is first pressurized
 119 above the granular material, leading to a gas pressure increase between the particles. After the
 120 valve is opened, the pressure of the air above the granular bed drops ([Fig. 2d–g](#) and [Fig. 3](#)). The
 121 pressure of the air in the bed itself drops in turn, but with a time delay that depends on the bed’s
 122 permeability, its total thickness and on the distance to the bed surface. The difference between
 123

124 the pressure within the bed and at its surface increases rapidly (Fig. 3b), creating a gas pressure
 125 gradient that can counterbalance the weight of the particles. For low decompression rates (e.g.
 126 < 2 kPa/s, see how this value is calculated in Methods), the gas pressure drops in the bed but
 127 no movement of the granular material is detected. For intermediate decompression rates
 128 (between 2 kPa/s and 8 kPa/s, Fig. 4a), the decompression causes an expansion of the granular
 129 material. Experiments with different slope angles show granular flow occurring even on a slope
 130 of a few degrees, which indicates partial fluidisation of the granular material. Bubbles can be
 131 observed in the bed. For high decompression rates (>8 kPa), the granular material exhibits very
 132 fluid behaviour: it flows even on very gentle initial slopes (5°) and forms waves that oscillate
 133 before coming to a standstill on a nearly horizontal surface (Fig. 3c). Bubbles, whose size
 134 increases with the decompression rate, form in the granular bed and burst at its surface (Fig.
 135 3f–g) forming degassing craters.



136 **Figure 3:** Results of the decompression experiments. (a) Evolution of the pressure with an initial slope of 10° (d,
 137 e and f), an initial overpressure P_{s0} of 25 kPa and a maximal decompression rate of ~ 11 kPa/s (mean 5 kPa/s) for
 138 the three sensors shown in (d). The letters in the black circles refer to the locations of figures d–g. (b) Gas pressure
 139 difference between sensors 3 and 8, and the granular bed surface (sensor 1). The horizontal dashed lines show the
 140 pressure difference needed to fully fluidise the flows, or to enable flow on a 10° slope. (c) Evolution of the slope
 141 with time, from an initial angle of 10° to horizontal after fluidisation. (d) Initial geometry of the granular bed
 142 before decompression. (e) Flow of the granular bed before bubble genesis. (f) Bubble formation. The
 143 decompression rate makes that only the top half of the bed is able to fully fluidise (see caption (b)). (g) Full
 144 fluidisation of the whole granular bed and high bubble formation at lower initial pressure (17 kPa) but with a
 145 higher decompression rate (79 kPa/s).
 146
 147

148 Movies of some experiments synchronized with pressure data are given in [Data availability](#).
 149 Similar results have been obtained using natural material at high temperature (>100°C).
 150 However, below 100°C, the natural material is very sensitive to temperature, probably due to
 151 interaction with air humidity, and cohesive behaviour can be observed: cracks form during
 152 decompression that coalesce to form preferential paths by which the gas escapes, carrying with
 153 it the smallest particles and forming fine-depleted degassing pipes while reducing the
 154 effectiveness of fluidisation.

155 **Numerical simulation of the fluidisation**

157 To explore the whole ranges of unloading (i.e. decompression) conditions (P_{s0} , Δt , μ) and of
 158 deposit characteristics (K , H , ρ) defined in the section [Range of parameters studied](#), we have
 159 written a numerical model for defluidisation (downloadable in [Code availability](#)) inspired by
 160 the work of ref³⁵. We have validated the numerical model against our experimental results in
 161 terms of the evolution of the pressure with time and the capacity of the granular bed to flow on
 162 a slope. Then we have used the model to explore a broader range of conditions (see [Methods](#)
 163 and [Extended Data Fig. 1](#)).

164 Analysis of the numerical results shows that the system is controlled by two dimensionless
 165 numbers. $\Pi_1 = \frac{\rho g H}{P_{s0}}$ controls the maximal depth of fluidisation with respect to the PDC

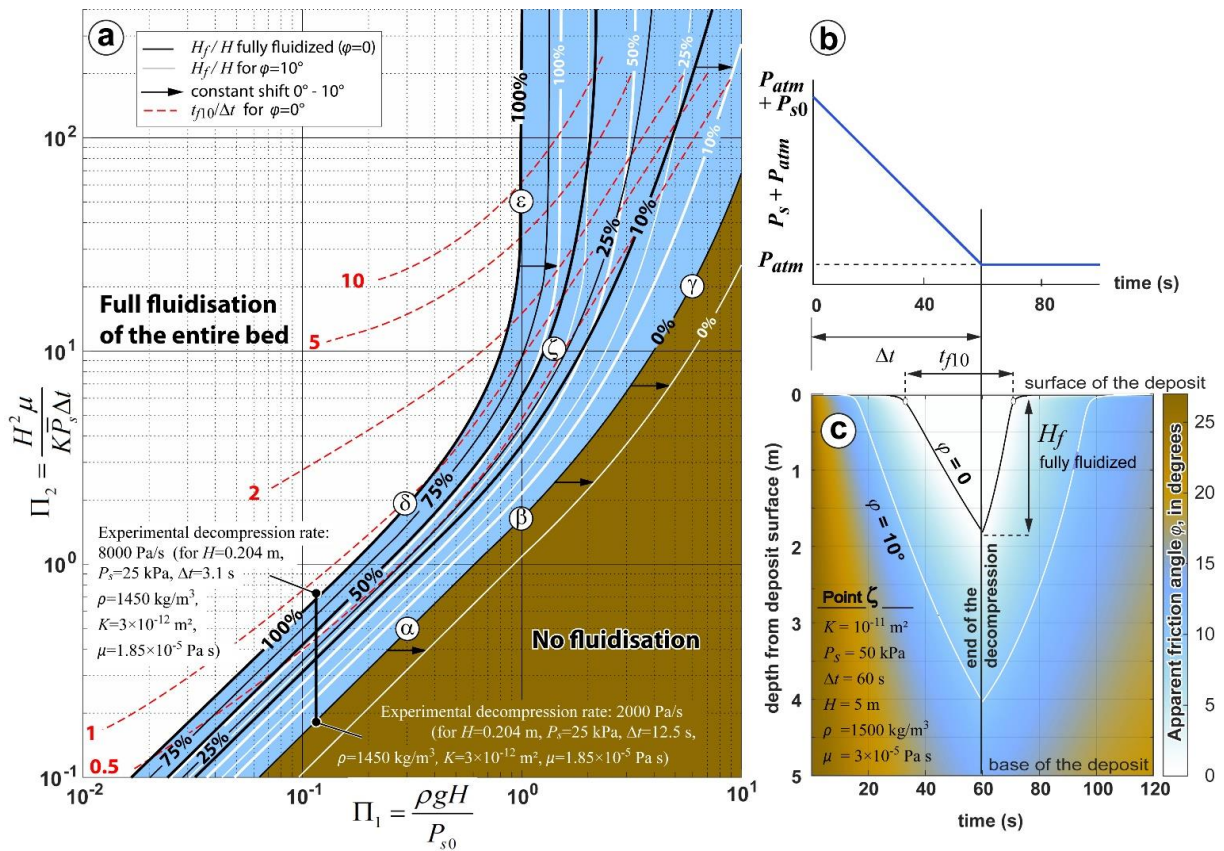
166 pressure, with g as gravity. $\Pi_2 = \frac{H^2 \mu}{K \bar{P}_s \Delta t}$ is a ratio of the characteristic defluidisation time of the

167 granular bed over the unloading time Δt of the dilute PDC, with \bar{P}_s the mean value of gas
 168 pressure during unloading approximated by $\bar{P}_s = P_{atm} + P_{s0}/2$ (see [Methods](#)).

169
 170 The maximal gradient of the gas pressure is systematically at the surface of the granular bed
 171 and this explains why the fluidisation (number of bubbles and granular flow) is higher at the
 172 surface of our experiments than at the bottom. We use the term ‘full fluidisation’ where the
 173 pressure gradient of the gas equals that of the particles and where, consequently, friction
 174 between the particles is zero. Full fluidisation can affect the entire bed or the upper part alone.
 175 [Fig 4a](#) (and [Extended Data Fig. 2](#)) shows the ratio H_f/H of the fully fluidised depth, H_f ,
 176 (from the surface) over the total bed thickness, H , according to Π_1 and Π_2 . $\Pi_1 = 1$ is the limit
 177 for the full fluidisation of the entire bed and, at higher values (thicker deposits or lower
 178 pressures), the upper part of the granular material alone is fluidised.

179 A thin or very permeable deposit loses its gas rapidly (dark grey domain, [Fig. 4a](#)) while a thick
 180 or low permeability deposit (light grey and white domains) retains the gas longer, maintaining
 181 the pressure difference needed for full fluidisation of its upper part. Analysis of Π_1 and Π_2
 182 shows that low permeability deposits ($K = 10^{-12} \text{ m}^2$) are fluidised relatively easily except at low
 183 thicknesses (<10 cm) or over long unloading times. For example, with $P_{s0} = 10 \text{ kPa}$, $\rho = 1500$
 184 kg/m^3 and $\mu = 3 \times 10^{-5} \text{ Pa s}$, a deposit of 20.4 cm, 68 cm and 4 m experiences full fluidisation at
 185 its surface for unloading times, Δt , of less than 23s, 76s and 234 s respectively ([Fig. 4a](#), point
 186 α : $\Pi_1=0.3$ and $\Pi_2=0.5$, point β : $\Pi_1=1$ and $\Pi_2=1.7$, point γ : $\Pi_1=6$ and $\Pi_2=20$). For $\Pi_1=0.3$, the
 187 deposit is entirely fluidised for $\Pi_2 > 2$, i.e. for $\Delta t < 5.8\text{s}$. [Figure 4a](#) also gives the values of $t_{f10}/\Delta t$
 188 , the ratio of t_{f10} (the period of full fluidisation of the upper 10 centimetres of the granular bed,
 189 [Fig. 4c](#)), over the unloading time. In extreme cases, the bed can remain fluidised for several
 190 minutes after the passage of the dilute PDC. For example, with $H=5\text{m}$, $\rho=1000 \text{ kg/m}^3$ and P_{s0}
 191 $= 50\text{kPa}$, $\Pi_1 = 0.98$ (point ϵ). With $K=10^{-12} \text{ m}^2$ and $\Delta t=120 \text{ s}$, $\Pi_2 = 49.5$. The deposit is thus

192 fluidised over nearly its whole thickness and $t_{f10}/\Delta t \approx 8$ indicates that the upper 10 centimetres
 193 are fluidised for more than 15 minutes by gas escaping from below.
 194 The higher permeabilities ($K = 10^{-11} \text{ m}^2$) require thicker deposits, higher pressures or shorter
 195 unloading times to achieve fluidisation, but a significant depth of material can become fully
 196 fluidised. For example, with $P_{s0} = 50 \text{ kPa}$, $\Delta t = 60 \text{ s}$ and $\rho = 1500 \text{ kg/m}^3$ (Fig. 4b–c), 35% of the
 197 deposit is fully fluidised (i.e. down to a depth of 1.75 m) for a deposit thickness of 5 m (point
 198 ζ : $\Pi_1 = 1.47$, $\Pi_2 = 9.90$). The upper 10 centimetres are fully fluidised for about 40 s ($t_{f10}/\Delta t$
 199 $\approx 66\%$). Finally, it should be noted that full fluidisation is not required to initiate a flow. For the
 200 previous example ($H = 5 \text{ m}$, $P_{s0} = 50 \text{ kPa}$, $\Delta t = 60 \text{ s}$), the upper 10 cm can flow for 80 s on a 10°
 201 slope and 80% of the deposit thickness (i.e. 4 m) can be remobilized ($\varphi = 10^\circ$, white line Fig.
 202 4c, see Methods for explanation of the apparent friction angle φ). The prediction of the deposit
 203 thickness that can flow on a given slope is predicted by a shift in the curves (white curves, Fig
 204 4a).
 205



206
 208 **Figure 4:** Results of the numerical study of the fluidisation by the unloading of a dilute PDC. (a) Evolution of the
 209 ratio H_f/H using to Π_1 and Π_2 . The black curves give the values of H_f/H for a full fluidisation ($\varphi=0^\circ$).
 210 The white curves, which are slightly shifted black curves, give H_f/H that flow on a 10° slope ($\varphi=10^\circ$). The
 211 dashed curves give the value of $t_{f10}/\Delta t$. Greek letters refer to explanations in the text. The two experimental
 212 decomposition rates used as examples in the text are also reported ($\Pi_1 = 0.116$). (b) Evolution of the gas pressure
 213 imposed at the surface of the deposit for point ζ . (c) Evolution of the friction angle of the deposit with time for
 214 $P_{s0}=50 \text{ kPa}$, $K=10^{-11} \text{ m}^2$ and $\Delta t=60 \text{ s}$ (point ζ). Total fluidisation ($\varphi = 0$) affects a depth of 1.75 m and the upper
 215 part of the deposit is fluidised for 40 s. Material can flow down slopes greater than 10° to a maximal depth of 4 m
 216 and the upper 10-cm can flow over this slope for about 80 s.

220 **Implications of large-scale fluidisation**

221 The capacity of a dilute PDC to trigger remobilisation of the underlying deposits is mainly
222 related to the permeability of the deposit and, consequently, the size of its particles^{38,45}. We
223 show that for a permeability of 10^{-12} m² or less, realistic conditions of dilute PDC unloading
224 and deposit thickness are compatible with deposit fluidisation and resulting concentrated flow
225 on a slope. For a permeability of more than 10^{-11} m², full fluidisation only occurs at the surface
226 of thick deposits (>1 m). Are these conditions realistic for volcanic environments? Deposits in
227 nature are rarely emplaced onto an impermeable basement and instead tend to be emplaced onto
228 volcanoclastic deposits from previous activity (ash fall or PDC deposits). When the dilute PDC
229 flows over such deposits, its pressure diffuses down into them, and they can exhibit the
230 behaviour described above after the unloading due to the passage of the current. Thus, 10, 20
231 or 50 cm of a deposit can be totally fluidised for a period of tens of seconds if a dilute PDC
232 moves over a thick sequence of previous permeable deposits.

233 We conclude that deposit fluidisation by dilute PDC unloading could be a relatively common
234 phenomenon. We think that it was the cause of the concentrated surge-derived pyroclastic flows
235 observed at Montserrat in 1997^{14,15} and our model is fully compatible with the ‘ash boiling’
236 described¹⁵. It is also compatible with observations at Ubehebe Crater^{13,19} and particularly the
237 conclusion that the deposit was inflated and soft shortly after deposition¹⁹. The fact that surge-
238 derived pyroclastic flows are not very commonly described in the literature is probably due to
239 the difficulty of identifying them, since the topography generally causes these secondary
240 concentrated flows to move into channel bottoms and blend with primary concentrated flows
241 in process, making it difficult to distinguish between the two. Our study proposes a new
242 physical framework for the interpretation of this kind of deposits. Note that our mechanism is
243 still compatible with local preservation of the sedimentary structures (dune, lamination, etc.)
244 observed in the field: it affects the deposit after deposition and only where the unloading
245 conditions are compatible with fluidisation.

246 The capacity for remobilization by the new mechanism revealed by our study is limited by
247 particle cohesion, which is rapidly increased by rain or atmospheric humidity. In these
248 conditions, the gas escapes through fractures, limiting the possibility for particles to flow, as
249 shown in the low temperature ignimbrite experiments. Thus, it seems unlikely that a PDC could
250 remobilize very large volumes of soil or old volcanic deposits. However, during an eruptive
251 phase, the particles might not be affected by atmospheric humidity. Each dilute PDC can pass
252 over several square kilometres of deposit^{8,9,11,20,40,41}. If thicker, denser or faster-moving PDC
253 develops, fluidisation conditions can be reached. Huge volumes of material accumulated over
254 large areas during a period of a number of days could suddenly be remobilized over an area of
255 several square kilometres. Thick concentrated flows of fine particles could then be generated
256 across the whole area covered by the dilute PDC and could reach long distances with little
257 warning on volcanic slopes, destroying areas previously considered to be safe. Volcanic
258 phenomena are complex and unknown mechanisms clearly pose a challenge for hazard
259 assessment. Our study shows that a dilute PDC can mobilize significantly more material than it
260 has deposited. This new hazard and the associated risks must be taken into account for future
261 estimates of volcanic threats.

262

263 **Acknowledgements**

264 This is contribution no. 590 of the ClerVolc program of the International Research Center for
265 Disaster Sciences and Sustainable Development of the University Clermont Auvergne. We
266 thank Thierry Latchimy, Edouard Régis, Eric Brut, Jean-Louis Fruquière and Cyrille Guillot
267 for their help in the construction of the experimental devices. The comments of Pr. Greg
268 Valentine contributed significantly to the improvement of the article.

269

270 **Author contributions**

271 Conceptualization: K.K. Laboratory experiments: K.K. & A.P. Numerical code: K.K.
272 Writing—original draft: K.K. & A.P. Writing—review and editing: K.K. Funding acquisition:
273 K.K.

274
275 **Competing interests Statement**

276 The authors declare that they have no known competing financial interests or personal
277 relationships that have influenced the work reported.

278
279 **Figure captions**
280

281 **Figure 1.** Emplacement of a dilute PDC. (a) The pressure of the gas, at its base, is higher than
282 atmospheric pressure. Consequently, it is higher in the resulting deposit. This induces deposit
283 fluidisation in the aftermath of the PDC, when the surface pressure drops back down rapidly
284 enough.

285
286 **Figure 2:** The experimental device made to simulate the unloading of a dilute PDC. (a) (1) the
287 sealed tank partially filled with granular material, (2) pump, (3) vertical pipe filled with water
288 for sensor calibration, (4) acquisition device, (5) computer and our dedicated acquisition
289 software, (6) LED for synchronisation of videos and pressure measurements, (7)
290 depressurisation valve, (8) pierced caps. (b) Locations of the pressure sensors, numbered 1–8.
291 (c) Schematic representation of one of the sensors used to measure the gas pressure at various
292 depths in the granular bed (located on 2b). (d) Initially, the air between the particles and that
293 above is at atmospheric pressure. (e) The air is then pressurised (using a pump (2) in (2a) and
294 diffuses between the particles. (f) When the pressure is equalized, the valve (7) in (2a) is opened.
295 A cap (8) in (2a) screwed on to the valve controls the decompression rate. Decompression is
296 slower between the particles than above them. (g) This creates a pressure gradient that can
297 fluidise the particle bed.

298
299 **Figure 3:** Results of the decompression experiments. (a) Evolution of the pressure with an
300 initial slope of 10° (d, e and f), an initial overpressure P_{s0} of 25 kPa and a maximal
301 decompression rate of ~ 11 kPa/s (mean 5 kPa/s) for the three sensors shown in (d). The letters
302 in the black circles refer to the locations of figures d–g. (b) Gas pressure difference between
303 sensors 3 and 8, and the granular bed surface (sensor 1). The horizontal dashed lines show the
304 pressure difference needed to fully fluidise the flows, or to enable flow on a 10° slope. (c)
305 Evolution of the slope with time, from an initial angle of 10° to horizontal after fluidisation. (d)
306 Initial geometry of the granular bed before decompression. (e) Flow of the granular bed before
307 bubble genesis. (f) Bubble formation. The decompression rate makes that only the top half of
308 the bed is able to fully fluidise (see caption (b)). (g) Full fluidisation of the whole granular bed
309 and high bubble formation at lower initial pressure (17 kPa) but with a higher decompression
310 rate (79 kPa/s).

311
312 **Figure 4:** Results of the numerical study of the fluidisation by the unloading of a dilute PDC.
313 (a) Evolution of the ratio H_f/H using to Π_1 and Π_2 . The black curves give the values of
314 H_f/H for a full fluidisation ($\varphi=0^\circ$). The white curves, which are slightly shifted black curves,
315 give H_f/H that flow on a 10° slope ($\varphi=10^\circ$). The dashed curves give the value of $t_{f10}/\Delta t$.
316 Greek letters refer to explanations in the text. The two experimental decompression rates used
317 as examples in the text are also reported ($\Pi_1 = 0.116$). (b) Evolution of the gas pressure imposed
318 at the surface of the deposit for point ζ . (c) Evolution of the friction angle of the deposit with
319 time for $P_{s0}=50$ kPa, $K=10^{-11}$ m² and $\Delta t=60$ s (point ζ). Total fluidisation ($\varphi = 0$) affects a depth

320 of 1.75 m and the upper part of the deposit is fluidised for 40 s. Material can flow down slopes
321 greater than 10° to a maximal depth of 4 m and the upper 10–cm can flow over this slope for
322 about 80 s.

323

324 **References**

325

- 326 1. Sparks, R. S. J. & Walker, G. P. L. The ground surge deposit: a third type of
327 pyroclastic rock. *Nat. Phys. Sci.* 241(107), 62–64 (1973).
- 328 2. Valentine, G. A. Stratified flow in pyroclastic surges. *Bull. Volcanol.* 49(4), 616–630
329 (1987).
- 330 3. Branney, M. & Kokelaar, P. *Pyroclastic Density Currents and the Sedimentation of*
331 *Ignimbrites* Geological Society Memoir No. 27 (Geological Society, London, 2002).
- 332 4. Dufek, J., Esposti Ongaro, T. & Roche, O. Pyroclastic density currents: processes and
333 models. Chapter 35. Part IV Explosive Volcanism, *The Encyclopedia of Volcanoes*
334 (2015).
- 335 5. Andrews, B. J. & Manga, M. Experimental study of turbulence, sedimentation, and
336 coignimbrite mass partitioning in dilute pyroclastic density currents. *J. Volcanol.*
337 *Geoth. Res.* 225, 30–44 (2012).
- 338 6. Breard, E. C. P., Lube, G., Jones, J. R., Dufek, J., Cronin, S. J., Valentine, G. A., &
339 Moebis, A. Coupling of turbulent and non-turbulent flow regimes within pyroclastic
340 density currents. *Nat. Geosci.*, 9(10), 767–771 (2016).
- 341 7. Weit, A., Roche, O., Dubois, T., & Manga, M. Maximum solid phase concentration in
342 geophysical turbulent gas-particle flows: Insights from laboratory experiments.
343 *Geophys. Res. Lett.*, 46, 6388–6396 (2019).
- 344 8. Yamamoto, T., Takarada, S. & Shigeru S. Pyroclastic flows from the 1991 eruption of
345 Unzen volcano, Japan. *Bull. Volcanol.* 55, 166–175 (1993).
- 346 9. Cole, P. D. & al. Deposits from dome-collapse and fountain-collapse pyroclastic flows
347 at Soufriere Hills Volcano, Montserrat. In: Druitt, T. H. & Kokelaar, B. P. (eds) *The*
348 *Eruption of Soufriere Hills Volcano, Montserrat, from 1995 to 1999. Geological*
349 *Society, London. Memoirs*, 21, 231–262 (2002).
- 350 10. Bourdier, J. L., Boudon, G., & Gourgaud, A. Stratigraphy of the 1920 and 1929 nuée-
351 ardente deposits. Mt. Pelée, Martinique. *J. Volcanol. Geotherm. Res.* 38, 77–96
352 (1989).
- 353 11. Komorowski, J. C. & al. Paroxysmal dome explosion during the Merapi 2010 eruption:
354 Processes and facies relationships of associated high-energy pyroclastic density
355 currents. *J. Volcanol. Geotherm. Res.* 261, 260–294 (2013).
- 356 12. Douillet, G. A. & al. Syn- eruptive, softsediment deformation of deposits from dilute
357 pyroclastic density current: Triggers from granular shear, dynamic pore pressure,
358 ballistic impacts and shock waves. *Solid Earth*, 6, 553–572 (2015).
- 359 13. Valentine, G. A., Fierstein, J. & White, J.D.L. Pyroclastic deposits of Ubehebe Crater,
360 Death Valley, California, USA: Ballistics, pyroclastic surges, and dry granular flows.
361 *Geosphere*. 18 (6) 1926– 1957 (2022).
- 362 14. Calder, E. S. & al. Mechanisms of lava dome instability and generation of rockfalls and
363 pyroclastic flows at Soufriere Hills Volcano, Montserrat. In: Druitt, T.H. & Kokelaar,
364 B.P. (eds) *The Eruption of Soufriere Hills Volcano, Montserrat, from 1995 to 1999.*
365 *Geological Society, London, Memoirs*, 21. 173–190 (2002).
- 366 15. Druitt, T. H. & al. Small-volume, highly mobile pyroclastic flows formed by rapid
367 sedimentation from pyroclastic surges at Soufrière Hills Volcano, Montserrat: an
368 important volcanic hazard. *Geological Society, London, Memoirs*, 21, 263–279 (2007).

- 369 16. Fisher, R. V. Transport and deposition of a pyroclastic surge across an area of high
370 relief: the 18 May 1980 eruption of Mount St. Helens, Washington. *Geol. Soc. Am.*
371 *Bull.*, 102(8), 1038–1054 (1990).
- 372 17. Hoblitt, R. P., Miller, D. C. & Vallance, J. E. Origin and stratigraphy of the deposits
373 produced by the May 18 directed blast. In: Lipman, P.W. & Mullineaux, D.R. (eds) *The*
374 *1980 Eruptions of Mount St. Helens, Washington*. US Geological Survey, Professional
375 Papers, 1250, 379–400 (1981).
- 376 18. Fisher, R. V., Smith, A. L. & Roobol, M. J. Destruction of St. Pierre, Martinique, by
377 ash-cloud surges, May 8 and 20 1902. *Geology*. 8, 472-476 (1980).
- 378 19. Valentine, G. A., Fierstein, J. & White, J.D.L. Soft sediment deformation in dry
379 pyroclastic deposits at Ubehebe Crater, Death Valley, California. *Geology*. 49, 211–215
380 (2021).
- 381 20. Ritchie L. J., Cole, P. D. & Sparks R. S. J. Sedimentology of deposits from the
382 pyroclastic density current of 26 December 1997 at Soufrière Hills Volcano,
383 Montserrat. *Geological Society, London, Memoirs*, 21, 435 – 456 (2015).
- 384 21. Cummins, P. R. Irrigation and the Palu landslides. *Nat. Geosci.* 12, 881–882 (2019).
- 385 22. Bradley, K. & al. Earthquake-triggered 2018 Palu Valley landslides enabled by wet rice
386 cultivation. *Nat. Geosci.* 12, 935–939 (2019).
- 387 23. Watkinson, I. M. & Hall, R. Impact of communal irrigation on the 2018 Palu
388 earthquake-triggered landslides. *Nat. Geosci.* 12, 940–945 (2019).
- 389 24. Massey, C. & al. Landslides triggered by the 14 november 2016 Mw 7.8 Kaikōura
390 earthquake, New Zealand. *Bull Seismol, Soc Am.* 108(3B):1630–48 (2018).
- 391 25. Xu, C. & al. Landslides triggered by the 2016 Mj 7.3 Kumamoto, Japan, earthquake.
392 *Landslides* 15(3): 551–64 (2018).
- 393 26. Ishihara, K. & Koga, Y. Case Studies of Liquefaction in the 1964 Niigata Earthquake.
394 *Soils and Foundations*, 21(3), 35–52 (1981).
- 395 27. Yoshida, N. & al. Causes of Showa Bridge collapse in the 1964 Niigata earthquake
396 based on eyewitness testimony. *Soils and Foundations*. 47 (6): 1075–1087 (2007).
- 397 28. Sparks, R. S. J. Particle size variations in ignimbrites and implications for the transport
398 of pyroclastic flows. *Sedimentology*, 23:147–188 (1976).
- 399 29. Wilson, C. J. N. The role of fluidization in the emplacement of pyroclastic flows: an
400 experimental approach. *J Volcanol Geotherm Res* 8:231–249 (1980).
- 401 30. Druitt, T. H. Pyroclastic density currents. *Geol. Society London Spec. Publ.* 145, 145–
402 182 (1998).
- 403 31. Freundt, A. & Bursik, M. Pyroclastic flow transport mechanisms. In: Freundt A, Rosi
404 M (eds) *From magma to tephra*. Elsevier, pp 173-245 (2001).
- 405 32. Roche, O. Depositional processes and gas pore pressure in pyroclastic flows: An
406 experimental perspective. *Bull. Volcanol.* 74, 1807–1820 (2012).
- 407 33. Gueugneau, V., Kelfoun, K., Roche, O., & Chupin, L. Effects of pore pressure in
408 pyroclastic flows: Numerical simulation and experimental validation. *Geophys. Res.*
409 *Lett.*, 44, 2194– 2202 (2017).
- 410 34. Kelfoun, K. & Gueugneau, V. A unifying model for pyroclastic surge genesis and
411 pyroclastic flow fluidization. *Geophys. Res. Lett.*, 49 (5) (2022).
- 412 35. Druitt, T. H., Avard, G., Bruni, G., Lettieri, P. & Maez, F. Gas retention in fine-grained
413 pyroclastic flow materials at high temperatures. *Bull. Volcanol.* 69, 881–901 (2007).
- 414 36. Chedeville, C., & Roche, O. Autofluidization of collapsing bed of fine particles:
415 Implications for the emplacement of pyroclastic flows. *J. Volcanol. Geotherm. Res.*,
416 368, 91– 99 (2018).
- 417 37. Walker, G. P. Grain-size characteristics of pyroclastic deposits. *J. Geol.*, 79(6), 696–
418 714 (1971).

- 419 38. Breard, E. C. P. & al. The permeability of volcanic mixtures. Implications for
420 pyroclastic currents. *J. Geophys. Res. Solid Earth*, 124 (2019).
- 421 39. Bareschino, P., et al. Fluidization and de-aeration of pyroclastic mixtures: The
422 influence of fines content, polydispersity and shear flow. *J. Volcanol. Geotherm. Res.*,
423 164, (4), 284–292 (2007).
- 424 40. Kelfoun, K., & al. Simulation of block-and-ash flows and ash-cloud surges of the 2010
425 eruption of Merapi volcano with a two-layer model. *J. Geophys. Res.: Solid Earth*, 122
426 (6), 4277–4292, (2017).
- 427 41. Gueugneau, V., Kelfoun, K. & Druitt, T. H. Investigation of surge-derived pyroclastic
428 flow formation by numerical modelling of the 25 June 1997 dome collapse at Soufrière
429 Hills Volcano, Montserrat. *Bull. Volcanol.* 81 (2019).
- 430 42. Moore, J. G. & Rice, C. J. Chronology and character of the May 18, 1980, explosive
431 eruptions of mount St Helens. In: *Explosive volcanism: inception, evolution and*
432 *hazards*. National Academy Press, Washington, DC (1984).
- 433 43. Syarifuddin, M. & al. Estimating the velocity of pyroclastic density currents using an
434 operational dual-PRF radar. *J. Volcanol. Geotherm. Res.*, 424 (2022).
- 435 44. Brosch, E., & al. Destructiveness of pyroclastic surges controlled by turbulent
436 fluctuations. *Nat. Commun.* 12, 7306 (2021).
- 437 45. Geldart, D. (1973). Types of gas fluidisation. *Powder Technology.* 7(5), 285–292.

438

439 **Methods**

440 **Experimental fluidisation by decompression**

441 The experimental device is composed of an ~7 litre (length 40 cm, width 6 cm, height 30 cm)
442 sealed tank partly filled with granular material (Fig 2a–b). Experiments were carried out with
443 various thicknesses H (< 25 cm) of either particles from a natural deposit (ignimbrite from
444 Neschers³⁵) or glass beads with a granulometry close to the fine matrix of dilute PDC deposits
445 (40–70 μm). The air pressure inside the tank could be raised (via the “in” hole, Fig 2b) up to
446 $P_{s0} = 30$ kPa above atmospheric pressure (Fig. 2e–f). The pressurized air also pushed up a water
447 column in a connected vertical pipe, providing an independent check on the pressure of the tank
448 with an accuracy < 10 Pa. A valve located above the granular material allowed the air to be
449 decompressed to atmospheric pressure (“out” hole, Fig 2b). Decompression rates, from 0 to 100
450 kPa/s, were controlled by caps pierced with holes of different diameters and screwed onto the
451 valve. Seven pressure sensors were sunk into the granular material and measured the air
452 pressure P at different depths. An eighth sensor (sensor 1, Fig. 2b) measured the air pressure P_s
453 $+ P_{\text{atm}}$ above the particle bed. The pressure sensors were 86–005G–C (for sensors 1, 3, 5 and 8,
454 Fig 2b) and 86–015G–C (for the others) of TE–Connectivity, with a maximal pressure range of
455 5 psi (~ 34 kPa) and 15 psi (~ 103 kPa) respectively and an accuracy of ~ 23 Pa and ~ 70 Pa.
456 The sensors were recalibrated before each experiment with water levels in the vertical pipe to
457 correct for potential instrumental drift. The measurements were taken at 1000 Hz. An LED lit
458 up when acquisition was triggered to synchronize the measurements with the videos (25 Hz and
459 500 Hz). To make the bubbles more visible, some experiments were done with the box tilted
460 slightly backwards to force the bubbles to move across the tank window.

461 Because the decompression rate is quasi exponential, it varies with time. For a comparison with
462 the numerical results, the values given in the *Experimental Results* section are the mean value,
463 \bar{P}_s (defined as the point at which the air overpressure is half that of the initial overpressure).

464 The maximal decompression rate ranges from the mean value itself (for the highest
465 decompression rates) up to 3 times the mean value (for the lowest decompression rates). A total
466 of 270 experiments were carried out using the glass beads, varying the slope of the tank and/or
467 the granular bed (0, 2, 10, 15, 20°), the initial gas overpressure (from 5 to 30 kPa), the
468 decompression rate (0 to 100 kPa/s), the bed thickness (15, 20, 25 cm) and the temperature

469 (20°C to 60°C). A total of 50 experiments were carried out using the ignimbrite ($H=10$ cm to
 470 $H=20$ cm, slopes from 0 to 30°, temperature from 20°C to 150°C).

471

472 Numerical model

473 The numerical model follows the development of ref³⁵ and is given in [Code availability](#). We
 474 simplified the problem by assuming that the granular bed is non-expansive (as observed for
 475 slow decompression rates). Mass conservation of the gas implies that:

$$476 \quad \frac{\partial}{\partial t}(\varepsilon\rho_g) + \frac{\partial}{\partial z}(\varepsilon\rho_g u_g) = 0 \quad (1)$$

477 where t is time, ε the porosity of the granular bed, ρ_g is gas density, z the elevation and u_g the
 478 gas velocity in the pores. The velocity in the pores is related to the Darcy velocity u_D (i.e. the
 479 volumetric rate of flow per unit area) with:

$$480 \quad u_g = \frac{u_D}{\varepsilon} = -\frac{K}{\varepsilon\mu} \left(\frac{\partial P}{\partial z} - \rho_g g \right) \quad (2)$$

481 where μ is the gas viscosity, K is the gas permeability in the granular bed and g is gravity.

482 The link between the gas density ρ_g and its pressure P is deduced from the perfect gas law:

$$483 \quad \rho_g = \rho_{atm} \frac{P}{P_{atm}} \quad (3)$$

484 with ρ_{atm} the density of the air (1.2 kg/m³) at atmospheric pressure P_{atm} (101.3 kPa).

485

486 To reproduce the experiments, the initial overpressure $P_{s0}+P_{atm}$ was set for the whole deposit.
 487 Then, a decrease in surface pressure P_s+P_{atm} was imposed following the experimental
 488 measurements from sensor 1. The pressure evolution in the granular bed was calculated by
 489 solving equations 1, 2 and 3. We explored various values for the permeability K , constant or
 490 varying in time and space. Numerical results were then compared to the experimental results to
 491 estimate the value of K and its range of variation ([Extended Data Fig. 1](#)). For low decompression
 492 rates, the bed expansion was small (little variation in the volume of space between the grains)
 493 and the whole defluidisation process was simulated with a constant value of K (2×10^{-12} m² for
 494 glass beads and 3×10^{-12} m² for the ignimbrite). For higher decompression rates, which induce
 495 fluidisation, the model showed that although the permeability varied in time and space, it
 496 remained within a relatively small range of values (e.g. between 2 and 4×10^{-12} m² for most
 497 experiments with glass beads, [Fig. 4](#)) except for the highest decompression rates with a large
 498 pressure gradient and bubbles, where K sometimes temporarily reached more than 10^{-11} m².

499 To predict if the granular material remains stable or if it flows, we calculated the apparent
 500 friction angle φ . A granular material can be stable on a slope due to friction between its
 501 constituent particles. This is described by a mechanical property called the friction angle. The
 502 friction angle δ of the material used is $27^\circ \pm 0.5^\circ$ for the glass beads and $36^\circ \pm 0.5^\circ$ for ignimbrite.
 503 The pressure gradient of the gas, by partially or totally sustaining the weight of the particles,
 504 lowers the friction and the apparent friction angle φ is given by:

$$505 \quad \tan \varphi = \left(1 - \frac{P - (P_s + P_{atm})}{\rho g h} \right) \tan \delta \quad (4)$$

506 where P is the air pressure at depth h , P_s is the air overpressure at the bed surface (and at the
 507 base of the PDC) that decreases from P_{s0} to 0, g is gravity and ρ the mean density of the granular
 508 bed. With no gas pressure gradient, $\varphi = \delta$. This means that for slopes α of the bed surface lower
 509 than φ , non-cohesive material is stable. Above this value ($\alpha > \varphi$), it flows until stability is
 510 reached. The bed is fully fluidised above the depth h when the air pressure P rises sufficiently

511 to create a value of $P - (P_s + P_{atm})$ that is equal to the pressure of the particles above, so that φ
512 equals 0. The bed flows like a fluid in a slope.
513 [Fig. 4a](#), has been compiled using the results of 5000 simulations (shown in [Extended Data Fig.](#)
514 [2](#)), either by varying the parameters controlling the defluidisation (P_{s0} , H , ρ , K , μ , Δt) or by
515 choosing sets of parameters, automatically and randomly, that give the imposed values of Π_1
516 and Π_2 . We applied ranges of values characteristic of natural deposits for various parameters:
517 permeability ($K=10^{-13}$ to 10^{-10} m²), gas viscosity ($\mu = 1.85$ at 20°C and 4.5×10^{-5} at 950°C),
518 deposit thickness ($H = 10$ cm to 10 m), deposit density (ρ from 500 to 2000 kg/m³), unloading
519 times (Δt from 0 to 300 s) and basal overpressures of PDC (P_{s0} from 1 to 100 kPa). The surface
520 overpressure P_s decreases linearly from P_{s0} to 0 ([Fig. 4b](#)). The maximal depth of fluidisation
521 H_f , for $\varphi=0$ and $\varphi=10^\circ$ and the time of fluidisation of the upper 10 centimetres are then used to
522 calculate H_f/H and $t_{f10}/\Delta t$. \bar{P}_s , in the definition of Π_2 , is the mean value of the gas pressure
523 at the base of the PDC and acts on the defluidisation by changing the gas density through its
524 compressibility β . It is approximated by $\bar{P}_s = P_{atm} + P_{s0}/2$ but because the gas pressure in the
525 deposit changes in time and space in a non-linear way, this approximation induces an error in
526 the prediction of H_f/H of up to 20% for low thicknesses ($\Pi_2 < 1$) and between simulations
527 done at high and low pressure (see [Extended Data Fig. 2](#)).

530 [Data availability](#)

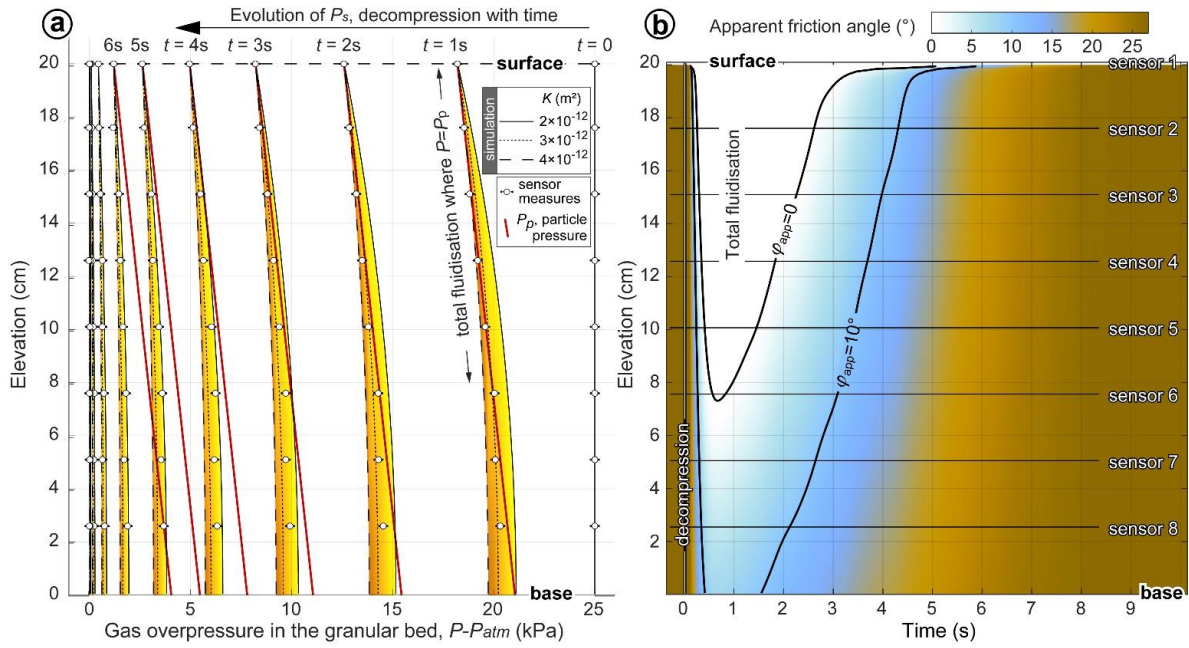
531 Videos and synchronized pressure data (text files) of characteristic experiments can be
532 downloaded here: <https://doi.org/10.25519/TF5A-8291>

535 [Code availability](#)

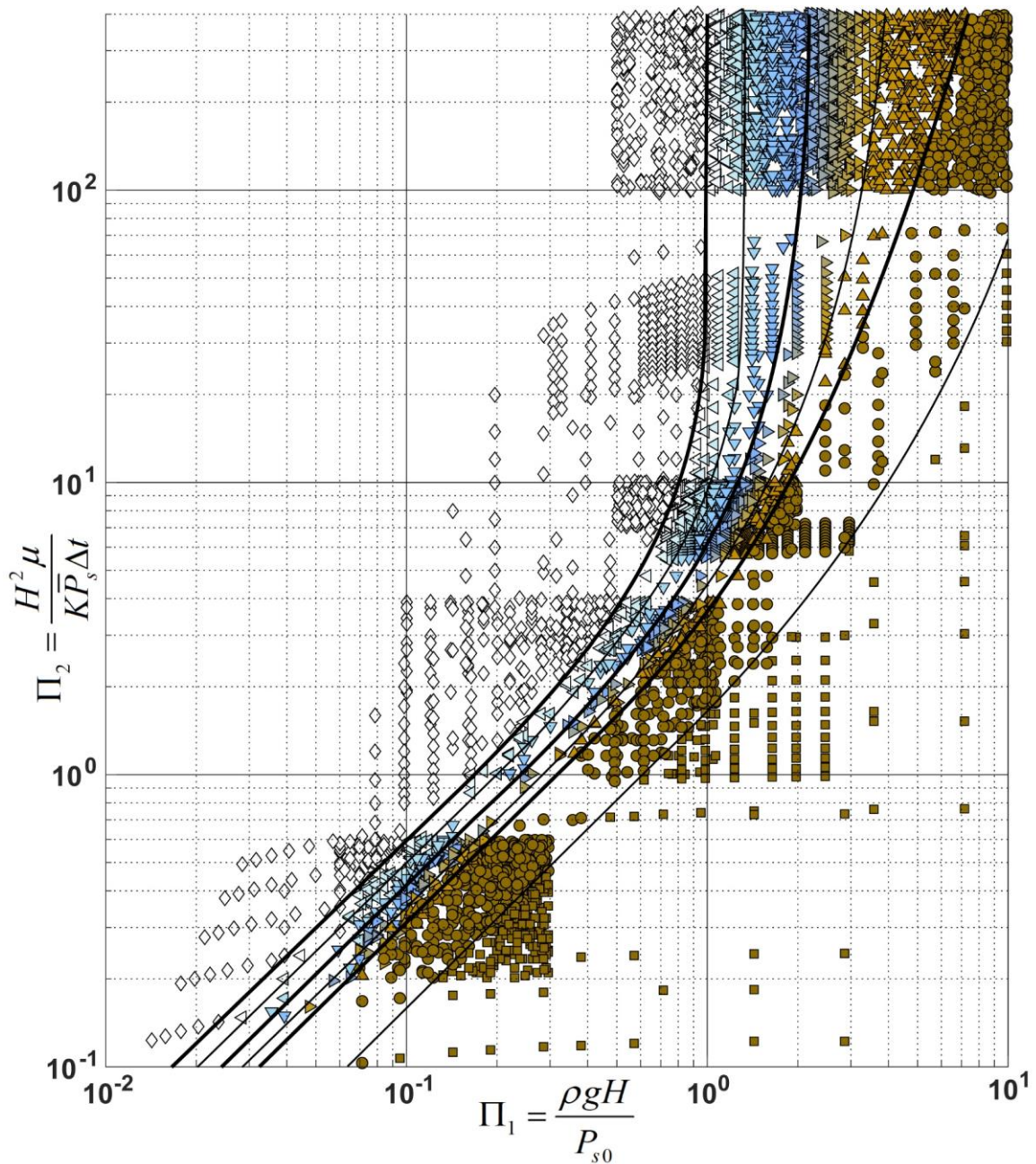
536 The numerical code used (open source) is available here: <https://doi.org/10.25519/TF5A-8291>
537 The estimation of the pressure and the decompression rate in the field has been done with the
538 version “Pyroclastic flows and surges” of VolcFlow downloadable here:
539 <https://lmv.uca.fr/volcflow/>

542 [Corresponding author](#)

543 Correspondence to Karim Kelfoun (karim.kelfoun@uca.fr)



560 **Extended data Figure 1:** Numerical simulation of one laboratory experiment. (a) Pressure evolution in the deposit
 561 for $K = 2 \times 10^{-12}$, 3×10^{-12} and 4×10^{-12} m². The experimental measurements are given by the white circles. Where the
 562 particle pressure is equal to or lower than the gas pressure, the granular material is fully fluidised locally. (b)
 563 Evolution of the apparent friction angle δ with time for $K = 3 \times 10^{-12}$ m². During decompression, the flow is fully
 564 fluidised down to about 12 cm beneath the surface and the apparent friction angle of less than 10° shows that all
 565 the material can flow on steeper slopes for more than 1 s (and the upper surface for 4 s). Because the geometry
 566 change induced by the flow was not simulated, results are compared with experiments carried out on the horizontal
 567 but the time of fluidisation coincides with the flow duration of experiments carried out on a slope and in the same
 568 conditions.
 569



570
 572
 573
 574
 575
 576
 577

Extended data Figure 2: Evolution of the ratio H_f/H according to Π_1 and Π_2 . The colours give the values of H_f/H of each of the 5000 simulations used to draw the curves (some points overlap exactly). The data used to make the figure are available here: <https://doi.org/10.25519/TF5A-8291>. They have been made with the numerical code available in the same repository.